

# Burning Thermals in Type Ia Supernovae

A. J. Aspden<sup>1</sup>, J. B. Bell<sup>1</sup>, S. Dong<sup>2</sup>, and S. E. Woosley<sup>2</sup>

## ABSTRACT

We develop a one-dimensional theoretical model for thermals burning in Type Ia supernovae based on the entrainment assumption of Morton, Taylor and Turner. Extensions of the standard model are required to account for the burning and for the expansion of the thermal due to changes in the background stratification found in the full star. The model is compared with high-resolution three-dimensional numerical simulations, both in a uniform environment, and in a full-star setting. The simulations in a uniform environment present compelling agreement with the predicted power-laws and provide model constants for the full-star model, which then provides excellent agreement with the full-star simulation. The importance of the different components in the model are compared, and are all shown to be relevant. An examination of the effect of initial conditions was then conducted using the one-dimensional model, which would have been infeasible in three dimensions. More mass was burned when the ignition kernel was larger and closer to the center of the star. The turbulent flame speed was found to be important during the early-time evolution of the thermal, but played a diminished role at later times when the evolution is dominated by the large-scale hydrodynamics responsible for entrainment. However, a higher flame speed effectively gave a larger initial ignition kernel and so resulted in more mass burned. This suggests that future studies should focus on the early-time behavior of these thermals (in particular, the transition to turbulence), and that the choice of turbulent flame speed does not play a significant role in the dynamics once the thermal has become established.

*Subject headings:* supernovae: general — white dwarfs — hydrodynamics — nuclear reactions, nucleosynthesis, abundances — conduction — methods: numerical — turbulence

---

<sup>1</sup>Lawrence Berkeley National Laboratory, 1 Cyclotron Road, MS 50A-1148, Berkeley, CA 94720

<sup>2</sup>Department of Astronomy and Astrophysics, University of California at Santa Cruz, Santa Cruz, CA 95064

## 1. INTRODUCTION

Type Ia supernovae are among the brightest explosions in the modern universe and are a useful tool for cosmological distance determination. It is generally agreed that they result from the thermonuclear explosion of a white dwarf accreting matter from a companion star in a binary system (Hoyle & Fowler 1960). The more specific nature of the progenitor though, be it a Chandrasekhar-mass white dwarf, sub-Chandrasekhar mass dwarf, or even two merging white dwarfs, is debated (e.g. Hillebrandt & Niemeyer 2000; Yoon et al. 2007; Sim et al. 2010), though most recent work has focused on the “single” Chandrasekhar-mass progenitor scenario.

Whatever the progenitor may be, the fact that a thermonuclear explosion is involved means that a realistic model requires an understanding of both the ignition and propagation of the burning. Barring a sudden detonation which, at least for the Chandrasekhar mass model, is ruled out by observations, the runaway proceeds through several stages. First compression raises the temperature to a point where local nuclear energy generation exceeds losses, e.g., by neutrino emission. Given the degeneracy of the electrons, the temperature continues to rise with the excess energy being carried away by convection. This phase may last centuries. Finally, subsonic convection is unable to carry all the energy and the temperature gradient steepens and becomes grossly superadiabatic. Again absent a detonation, the gradient continues to steepen until a small region runs away to very high temperature creating a sharp interface between fuel and ash called a “flame”. The subsequent rapid propagation of this flame causes the supernova.

In this paper, we focus on the Chandrasekhar mass model, though there are probably generalizations to the other models. Recent studies (e.g. Zingale et al. 2009, 2011) suggest that this sort of supernova will not usually ignite at its center. Instead, the initial burning is offset to one side by 30 - 90 km. Though small in comparison with the white dwarf size, about 1700 km, this displacement is sufficient for the supernova to burn only on one side (Niemeyer et al. 1996; Zingale & Dursi 2007; Röpke et al. 2007; Jordan et al. 2008). Because of the extreme temperature sensitivity of the nuclear energy generation, the burning probably begins as one or a few isolated hot spots, which we will represent here as a small sphere of ash. The surface of this sphere is deformed, perhaps grossly so, by the turbulence generated during the pre-explosive convection. Because of the burning and high temperature, the density of the bubble, under isobaric conditions, is smaller than its surroundings. It therefore floats and might be described as a “bubble”. As the bubble rises, instabilities develop on its perimeter while entrainment, burning, and expansion increase its mass and volume. Three-dimensional simulations of the bubble’s behavior are presented for physical conditions appropriate to the supernova, and an analytic model is developed to explain its late time evolution. The answers

obtained are very important to understanding the outcome of Type Ia supernova explosion models. Indeed, much of the diversity observed in Type Ia supernovae, both on the computer (Röpke et al. 2007; Jordan et al. 2008) and in nature (Kasen et al. 2009), probably results from different geometries of the ignition region and evolutions of the first plumes of burning as they rise to the surface of the star. We illustrate and validate our analytic model by comparing to a three-dimensional full-star model of a supernova (Dong et al. 2011).

Much use is made here of the rich literature in fluid mechanics concerning similar phenomena in the terrestrial context. In that literature, a localized blob of buoyant fluid is known as a thermal, which is considered a special case of a buoyant vortex ring; the difference being that the latter has initial momentum in addition to its buoyancy. Scorer (1957) investigated thermals experimentally, and proposed relations based on dimensional analysis of the form

$$z = nr \quad \text{and} \quad w = C(g\bar{B}r)^{1/2}, \quad (1)$$

where (using Scorer’s notation)  $z$  and  $r$  are the height and radius of the thermal,  $\bar{B}$  the mean buoyancy,  $w$  the vertical velocity,  $g$  acceleration due to gravity, and  $n$  and  $C$  are constants, where the latter is of the form of a Froude number.

Morton, Taylor, & Turner (1956) introduced the concept of an entrainment assumption. This approach considers an idealized thermal at time  $t$ , represented by a sphere of radius  $b(t)$  at a height  $z(t)$ , traveling vertically with speed  $u(t) = dz/dt$ . The entrainment assumption states that the entrainment at the edge of a thermal is proportional to some characteristic velocity within the thermal, which is usually taken to be  $u$ . Under the Boussinesq approximation, conservation equations for volume (or equivalently mass), momentum and buoyancy can be written as

$$\frac{d}{dt} \left( \frac{4}{3} \pi b^3 \right) = 4\pi b^2 \alpha u, \quad (2)$$

$$\frac{d}{dt} \left( \frac{4}{3} \pi b^3 (k_v \rho_e + \rho_i) u \right) = \frac{4}{3} \pi b^3 \beta (\rho_e - \rho_i) g, \quad (3)$$

$$\frac{d}{dt} \left( \frac{4}{3} \pi b^3 g \frac{\rho_e - \rho_i}{\rho_0} \right) = -\frac{4}{3} \pi b^3 u N^2, \quad (4)$$

where  $\alpha$  is the constant entrainment coefficient,  $\rho_i$ ,  $\rho_e$  and  $\rho_0 \equiv \rho_e(0)$  are the densities of the interior of the thermal, the ambient fluid and a reference density, respectively, and  $N^2 = -(g/\rho_0)(d\rho_e/dz)$  is the Brunt-Väisälä buoyancy frequency describing the ambient stratification. The first equation states that the rate of change of the total volume of the thermal is equal to the volume of the entrained fluid, i.e. the entrainment rate  $\alpha u$  times the surface area of the thermal. This is equivalent to rate of change of mass under the Boussinesq approximation. The second equation is just Newton’s second law, and states that the change

of momentum is equal to the total buoyancy force acting on the thermal. The ‘virtual mass coefficient’  $k_v$  has been included here to account for the momentum of the ambient fluid surrounding the thermal, which takes the theoretical value of one half for a rigid sphere, and we have also included an empirical constant  $\beta$ . The last equation describes the rate of change of buoyancy due to the density of the entrained fluid and background stratification. It follows immediately from equation (2) that  $b = \alpha z$ , for a suitably defined origin, as in equation (1). This means that the thermal prescribes a cone as it rises, regardless of the ambient conditions. For an unstratified ambient,  $\rho_e \equiv \rho_0$  and  $N^2 \equiv 0$ , the velocity from equation (1) can be easily derived.

Motivated by latent heat release in atmospheric clouds, Turner (1963) considered thermals where the buoyancy was enhanced due to chemical reaction. The experiments and analysis were restricted to two kinds of motion, either constant acceleration or constant velocity. We will see that the former case is relevant to burning thermals in SN Ia. A review of these early works can be found in Turner (1969).

In this paper, we consider applying this simple entrainment approach to an off-center ignition in SN Ia. Several effects have to be taken into consideration. The Boussinesq approximation is no longer appropriate due to the large variation in density. The effects of burning have to be considered, in particular changes in density and volume (and therefore buoyancy). Finally, the background stratification in a full star cannot be represented by a constant buoyancy frequency  $N$ , or even constant acceleration due to gravity  $g$ . We first consider the effects of burning in a uniform ambient to establish the applicability of the entrainment assumption to burning thermals, and establish values for the constants  $\alpha$  and  $\beta$ . A theoretical description is given and compared with new high-resolution numerical simulations. We then consider a burning thermal in a full-star setting. A theoretical description is given that extends the model to a non-uniform background, which is then compared with the high-resolution numerical simulations conducted by Dong et al. (2011). Each component of the one-dimensional model is examined and shown to be important to capture the behavior of the burning thermal in a full-star environment. The effect of initial conditions are then examined with the one-dimensional model by varying the initial radius, height, and flame speed of the thermal. More mass was burned when the ignition kernel was larger and closer to the center of the star. The turbulent flame speed was found to be important during the early-time evolution of the thermal, but played a diminished role at later times when the evolution is dominated by the large-scale hydrodynamics responsible for entrainment. However, a higher flame speed gave the effect of a larger initial ignition kernel and so resulted in more mass being burned.

## 2. THERMAL BURNING IN A UNIFORM AMBIENT

### 2.1. Analysis

To modify the analysis to account for the continual buoyancy increase due to heat release during burning, we assume that entrained fluid burns sufficiently quickly that the density inside the thermal can be treated as roughly constant in both time and space. Specifically, we can use the ‘top hat’ approach discussed in Morton et al. (1956), i.e. any point in space can be simply inside or outside the thermal. For uniform ambient, the outside density is a constant equal to the fuel density and burns to a constant ash density (instantaneously) upon entrainment. This means that there can only be two discrete densities, fuel  $\rho_F$  and ash  $\rho_A$ . This simplifies the equations as the Boussinesq approximation is no longer required (although the equations for volume and mass remain equivalent here because the densities are constant) and the buoyancy equation is redundant. Under these assumptions, the conservation equations (2)-(4) reduce to two equations for volume and momentum

$$\frac{d}{dt} \left( \frac{4}{3} \pi b^3 \right) = 4\pi b^2 \sigma \alpha u, \quad (5)$$

$$\frac{d}{dt} \left( \frac{4}{3} \pi b^3 (k_v \rho_F + \rho_A) u \right) = \frac{4}{3} \pi b^3 \beta (\rho_F - \rho_A) g, \quad (6)$$

where  $\sigma = \rho_F/\rho_A$  is the ratio of fuel and ash densities, and the acceleration due to gravity  $g$  is assumed to be a constant. Note the density ratio  $\sigma$  in equation (5) accounts for the expansion due to burning. Equivalently, the  $\rho_A$  can be included in the derivative on the left-hand side yielding a mass conservation equation. Again, note that the Boussinesq approximation has not been made here.

As before, it follows immediately that  $b = \sigma \alpha z$ , for a suitably defined origin, and so the burning thermal also prescribes a cone as it evolves. Substituting into equation (6) gives

$$\frac{d^2 z}{dt^2} + \frac{3}{z} \left( \frac{dz}{dt} \right)^2 = g', \quad (7)$$

where  $g' = g\beta(\rho_F - \rho_A)/(k_v \rho_F + \rho_A)$  is a constant reduced gravity. Equation (7) has the solution

$$z = \frac{g'}{14} t^2, \quad u = \frac{g'}{7} t, \quad \text{and} \quad b = \sigma \alpha z = \frac{\sigma \alpha g'}{14} t^2. \quad (8)$$

Equation 8 describes the self-similar evolution of a burning thermal. Note that this has the same form as the constant acceleration case considered by Turner (1963). A Froude number can be defined as

$$\text{Fr}^2 = \frac{u^2}{g' b},$$

which in the self-similar regime takes the value  $\text{Fr}_\infty^2 = 2/(7\sigma\alpha)$ . Moreover, an evolution equation for the Froude number can be derived

$$\frac{d}{dt}(\text{Fr}^2) = T(\text{Fr}_\infty^2 - \text{Fr}^2), \quad (9)$$

where  $T = 7\sigma\alpha u/b$ . This means that  $\text{Fr} = \text{Fr}_\infty$  is a stable equilibrium for positive  $u$ , i.e. the Froude number will tend towards  $\text{Fr}_\infty$  at late times.

To assess the applicability of such an entrainment model, we now compare this theoretical treatment with numerical simulations of a burning thermal in a uniform environment where the flame physics are well-resolved.

## 2.2. Numerical Approach

We use a low Mach number hydrodynamics code, adapted to the study of thermonuclear flames, as described in Bell et al. (2004). The advantage of this method is that sound waves are filtered out analytically, so that the time step is set by the the bulk fluid velocity and not the sound speed. This is an enormous efficiency gain for low speed flames. The input physics used in the present simulations is largely unchanged (we consider only carbon burning to magnesium), with the exception of the addition of Coulomb screening, taken from the Kepler code (Weaver et al. 1978), to the  $^{12}\text{C}(^{12}\text{C},\gamma)^{24}\text{Mg}$  reaction rate. This yields a small enhancement to the flame speed, and is included for completeness. The conductivities are those reported in Timmes (2000), and the equation of state is the Helmholtz free-energy based general stellar EOS described in Timmes & Swesty (2000). We note that we do not utilize the Coulomb corrections to the electron gas in the general EOS, as these are expected to be minor at the conditions considered.

Adaptive mesh refinement is achieved through a block-structured approach that uses a nested hierarchy of logically-rectangular grids with simultaneous refinement of the grids in both space and time, originally developed by Berger & Colella (1989); Bell et al. (1994). The integration algorithm on the grid hierarchy is a recursive procedure in which coarse grids are advanced in time, fine grids are advanced multiple steps to reach the same time as the coarse grids and the data at different levels are then synchronized. During the regridding step, increasingly finer grids are recursively embedded in coarse grids until the solution is sufficiently resolved. An error estimation procedure based on user-specified criteria evaluates where additional refinement is needed, and grid generation procedures dynamically create or remove rectangular fine grid patches as resolution requirements change. A coarse-grained parallelization strategy is used to distribute grid patches to nodes where the nodes communicate using MPI.

The non-oscillatory finite-volume scheme employed here permits the use of implicit large eddy simulation (ILES). This technique captures the inviscid cascade of kinetic energy through the inertial range, while the numerical error acts in a way that emulates the dissipative physical effects on the dynamics at the grid scale, without the expense of resolving the entire dissipation subrange. An overview of the technique can be found in Grinstein et al. (2007). Aspden et al. (2008) presented a detailed study of the technique using the present numerical scheme, including a characterization that allowed for an effective viscosity to be derived. Thermal diffusion plays a significant role in the flame dynamics, so it is explicitly included in the model, whereas species diffusion is significantly smaller, so it is not included.

The aim of this small-scale study is to establish the applicability of the entrainment model for a burning thermal using simulations where the flame physics are well-resolved. We consider a carbon-burning thermal (50% carbon, 50% oxygen) in a cubic domain of side length 864 cm with a free-slip base and outflow boundary conditions elsewhere. The fuel density was  $1.5 \times 10^7 \text{ g cm}^{-3}$ , which burned to an ash density of  $0.85 \times 10^7 \text{ g cm}^{-3}$ , hence  $\sigma = 1.76$ . Gravity was held constant at  $10^9 \text{ cm s}^{-2}$ . These conditions were chosen so that the flame was well-resolved at an accessible resolution, but the specific details are not expected to be important, as any self-similar evolution is independent of these factors. The thermal was initialized 54 cm above the bottom of the domain in the center, with a radius of approximately 14 cm and a significant perturbation to the surface to break symmetry. The density and temperature inside and outside the thermal were set equal to that of the ash and the fuel, respectively. The velocity was set to be zero throughout the domain. Adaptive mesh refinement was used to focus resolution on the thermal, lowering computational expense. Two simulations of burning thermals were run, differing only in resolution. The high resolution simulation, which we will refer to as Run H, had a base grid of  $512^3$ , with three levels of refinement, giving an effective resolution of  $4096^3$ . The theory predicts that the volume of the thermal grows with time to the sixth power, which means the refined region rapidly becomes large. Once the thermal had grown such that the simulation was prohibitively expensive, a level of refinement was removed, evolving the thermal at an effective resolution of  $2096^3$ . This step was repeated such that the final effective resolution was  $1024^3$ . We will refer to the three parts of the simulation as stages 1 through 3. The low resolution simulation, which we will refer to as Run L, had an effective resolution of  $2048^3$  from the beginning and was evolved through two stages in a similar manner to Run H. A third simulation was run under the same conditions at the same resolution as case H with the burning turned off to provide a comparison with conventional inert thermals.

### 2.3. Results

The early stages of development are depicted in figure 1 by three-dimensional renderings of burning (yellow) and magnitude of vorticity (blue) at nine time points between  $t = 0$  and 1.021 ms (for context the thermal reached to top of the domain after approximately 5.6 ms). All images are at the same scale and orientation; recall the initial radius is approximately 14 cm in a domain size of 864 cm. In the initial conditions, the burning is uniformly distributed over the surface of the thermal, and there is zero vorticity as the entire domain is stationary. As the thermal begins to rise, burning at the cap is extinguished by stretch induced by the large-scale flow around the thermal ( $t = 0.294$  ms). Thermodiffusive effects due to the high Lewis numbers lead to intense burning on the underside of the thermal ( $t = 0.421$  ms). Where the surface is deformed in such a way that the center of curvature is within the fuel, thermal diffusion focuses heat into the fuel, and so increases the burning rate. The curvature is maintained by the large-scale flow, and the intense burning region continues to burn upwards into the center of the thermal ( $t = 0.512$  ms). Eventually, this intense burning region is extinguished by the large-scale flow internal to the thermal ( $t = 0.722$  ms). As the thermal toruses ( $t = 0.821$  ms), the burning also occurs in toroidal structures, before secondary shear instabilities initiate the transition to turbulence ( $t = 0.919$ – $1.021$  ms).

Two-dimensional slices through the data shown in figure 2 compare the burning thermal (top row) at  $t = 2.042$  ms with the inert thermal (bottom row) at the same rise height. The four left-hand panels are horizontal slices, and the four right-hand panels are vertical slices. Both thermals have a toroidal structure, but the burning case has larger primary and secondary radii, and is considerably more asymmetric. The burning thermal has an almost bimodal temperature, close to the ash temperature inside, and fuel temperature outside. The vorticity is confined to this hot region, and is not present in the center, the inert thermal has vorticity distributed across the entire structure. The inert thermal has a strong and persistent coherent toroidal vortex core, which is not present in the burning case. Burning appears to suppress the transition to turbulence and self-similar evolution, and the burning thermal expands sideways more rapidly than in the inert case.

Three-dimensional renderings of temperature in figure 3 depict the thermal evolution over the later times of the simulation. All images are shown at the same scale, and the first image is close in time (and therefore size) to the final image from figure 1, which, contrasted with the image at ( $t = 5.258$  ms) highlights the rapid growth of the thermal after the transition to turbulence. A local extinction event occurs around  $t = 2.886$  ms (in the lower left of the image as shown), which leaves behind a coherent vortex structure that persists for the remainder of the simulation. However, the burning continues throughout the rest of the thermal, which dominates the overall evolution.

Two-dimensional slices through the data at  $t = 3.811$  ms (figure 4) show the distributions of temperature, magnitude of vorticity, and burning, left-to-right, respectively. By this stage of the evolution, the thermal has become fully-developed, with burning and vorticity distributed across the entire body of the thermal. The temperature field shows that the thermal still consists of regions of pure ash separated from pure fuel by relatively narrow mixing regions. This differs from the distribution expected from an inert thermal (see figure 2), where mixing leads to a broader distribution of temperature than the almost bimodal distribution seen in here, and is entirely due to burning: the entrained fuel quickly burns to the ash temperature. The distribution of burning across the thermal is of particular interest. Under these conditions, the burning occurs in pockets roughly evenly distributed across the whole thermal. This is indicative that the flame is dominated by the hydrodynamics, in particular, turbulent entrainment, rather than flame propagation driven by thermal diffusion. These observations support the assumptions that the burning thermal can be considered to be at the constant ash density, and that entrained fluid burns essentially instantaneously; the reactions are controlled by turbulent mixing.

If the one-dimensional entrainment model developed in the previous section is appropriate, then once the thermal has become fully-developed, a self-similar evolution should be observed, where the relations predicted by equation 8 should be satisfied, from which the model constants  $\alpha$ ,  $\beta$ , and virtual space-time origin  $(z_v, t_v)$  can be identified. To compare the three-dimensional simulations with the one-dimensional entrainment model, the thermal radius and height (and therefore velocity) were evaluated as a function of time. This was achieved by integrating over the entire computational domain and classifying each point in space as either inside or outside of the thermal based on a critical value of density. Specifically, any point in space with density below  $1 \times 10^7$  g cm<sup>-3</sup> was considered to be inside the thermal, and otherwise outside the thermal. This defines a volume  $V$  over which the integrals of 1,  $\rho$  and  $\rho z$  were evaluated. The first two quantities respectively define the volume and mass of the thermal, and the latter, when divided by the mass, defines the vertical center of mass of the thermal, taken to be the thermal height. The radius was taken to be that of a sphere with volume equal to that of the thermal, i.e.  $b = (3V/4\pi)^{1/3}$ .

To establish if the entrainment model is indeed appropriate, the data were compared with the predicted power-law evolution. The entrainment coefficient  $\alpha$  and virtual space origin  $z_v$  were first evaluated by performing a least-squares best-fit to the radius as a function of height, taking data after the thermal has become fully-developed, i.e.  $t \gtrsim 2.05$  ms. Specifically, given a value of  $\sigma = \rho_F/\rho_A$ ,  $\alpha$  and  $z_v$  were found by a best-fit to  $b = \alpha\sigma(z - z_v)$ . The shape function  $\beta$  and virtual time origin  $t_v$  were evaluated by a best-fit to the thermal height as a function of time, i.e.  $\sqrt{z - z_v} = \sqrt{g'/14}(t - t_v)$ , where the value for  $\beta$  is obtained implicitly through  $g'$ . The best-fits were performed for both cases H and L. The normalized height as a

function of radius and square root of normalized height as a function of normalized time are presented in figure 5. The data from the simulations are presented as symbols (not all data points have been presented for clarity), where each kind of symbol corresponds to the various stages of each simulation, note the overlap of data, confirming the validity of the choice of continuation points. In both figures, the agreement with the predicted power-law behavior is compelling; height as a function of time is particularly robust ( $\beta = 0.50$ ). There is a slight difference with resolution in the entrainment coefficient:  $\alpha = 0.17$  for case H, and  $\alpha = 0.19$  for case L, but this is well within the range observed in the laboratory experiments of Turner (1963) with constant acceleration (0.14-0.26), although we note that we have adjusted for the density ratio  $\sigma$ . We will use the values  $\alpha = 0.17$  and  $\beta = 0.50$  for the full-star model.

### 3. THERMAL BURNING IN A FULL STAR

#### 3.1. Analysis

We now consider the evolution of a burning thermal in a full-star, specifically to include the effect of the pressure gradient. First, we require equations to describe the background stratification, which we take to be spherically symmetric, we use  $z$  to denote height to avoid confusion with the radius of the thermal. For simplicity, we describe the equation of state solely by a relativistic degenerate electron pressure given by a polytrope of order  $n = 3$ . Specifically, write pressure  $p_F(z)$  as a function of density  $\rho_F(z)$  according to

$$p_F = K(Y_e \rho_F)^\gamma, \quad \gamma = 1 + \frac{1}{n} = \frac{4}{3}, \quad (10)$$

where  $Y_e = 1/2$  and  $K = 1.244 \times 10^{15} \text{ dyne cm}^{-2}$ . We assume the star is in hydrostatic equilibrium,

$$\frac{dp_F}{dz} = -\rho_F g, \quad (11)$$

and  $g(z)$  is given by Newton's law of universal gravitation

$$g(z) = \frac{4\pi G}{z^2} \int_0^z \rho_F \eta^2 d\eta, \quad (12)$$

where  $G = 6.67 \times 10^{-8} \text{ cm}^3 \text{ g}^{-1} \text{ s}^{-2}$ . Combining equations (10)-(12), and assuming  $\rho_F$  is finite at  $z = 0$ , a single second-order non-linear ordinary differential equation can be obtained for density as a function of height

$$\frac{1}{\rho_F z^2} \frac{d}{dz} \left( \rho_F^{\gamma-2} z \frac{d\rho_F}{dz} \right) = -\frac{4\pi G}{\gamma K Y_e^\gamma}. \quad (13)$$

In non-dimensional form, equation (13) is the Lane-Emden equation, which is known not to possess an analytic solution for  $n = 3$ . This means a simple solution of the kind found in the previous sections will not be forthcoming, and that numerical integration will be required to find a semi-analytic solution for a burning thermal in such an environment.

We now derive conservation equations for volume, mass and momentum for a burning thermal of density  $\rho$  rising in an ambient stratification of density  $\rho_F$  satisfying (13). A power law is used to describe the ash density  $\rho_A$  as a function of fuel density  $\rho_F$ , given by  $\rho_A = 0.1168, rho_F^{1.091}$ , where the constants were determined from a least-squares best-fit to data from Timmes & Woosley (1992) and Woosley (2007). The Boussinesq approximation is not appropriate due to large variations in density, which means the equations for volume and mass are no longer interchangeable. As before, we assume that the thermal entrains fluid at a rate proportional to the rise speed, and that the entrained fluid mixes and burns instantaneously. The entrainment coefficient is assumed to be constant. In this case, we also allow the thermal to burn independently from entrainment by adding a flame speed  $s$  to the rate of entrainment, i.e. the total rate of entrainment is taken to be  $\alpha|u| + s$ . This is necessary due to the large turbulent flame speed used in the full-star simulation, and was not required in the previous section because the laminar flame speed is much slower. This is particularly important when the thermal is stationary, but continues to burn outwards, which is not captured by the entrainment assumption. The final assumption is that the thermal rises isentropically and instantaneously expands and equilibrates to the ambient pressure at that height. The change of specific volume  $\tau$  associated with this expansion can be written as

$$\frac{d\tau}{dt} = -\frac{\tau}{\rho_F} \frac{d\rho_F}{dt}. \quad (14)$$

This means that conservation equations for volume, mass and momentum can be written as

$$\frac{d}{dt} \left( \frac{4}{3} \pi b^3 \right) = 4\pi b^2 \sigma (\alpha|u| + s) - \frac{4\pi b^3}{3\rho_F} \frac{d\rho_F}{dt}, \quad (15)$$

$$\frac{d}{dt} \left( \frac{4}{3} \pi b^3 \rho \right) = 4\pi b^2 \rho_F (\alpha|u| + s), \quad (16)$$

$$\frac{d}{dt} \left( \frac{4}{3} \pi b^3 (k_v \rho_F + \rho) u \right) = \frac{4}{3} \pi b^3 \beta (\rho_F - \rho) g. \quad (17)$$

The two terms on the right-hand side of equation (15) account for the change in volume of the thermal due to burning (as in the previous section) and isentropic expansion (following equation (14)), respectively. Equation (16) states that the total mass of the thermal increases by the mass of the entrained fuel. Finally, equation (17), as before, is Newton's second law

and describes the rate of change of momentum due to buoyancy. An equation for conservation of buoyancy can be derived, but is not required.

Assuming that the rise of the thermal does not affect the background stratification, and combining equations (12), (13), and (15)-(17) with the expression for burning and  $u = dz/dt$  (which is used as a change of variable from  $z$  to  $t$  where necessary), the entire system can be described by a system of six non-linear ordinary differential equations, which can be written in terms of primitive variables as

$$\frac{dz}{dt} = u, \quad (18)$$

$$\frac{dg}{dt} = 4\pi G\rho_F u - \frac{2gu}{z}, \quad (19)$$

$$\frac{d\rho_F}{dt} = -\frac{gu}{\gamma KY_e^\gamma \rho_F^{\gamma-2}}, \quad (20)$$

$$\frac{db}{dt} = \sigma(\alpha|u| + s) + \frac{bgu}{3\gamma KY_e^\gamma \rho_F^{\gamma-1}}, \quad (21)$$

$$\frac{d\rho}{dt} = \frac{3\sigma(\alpha|u| + s)}{b}(\rho_A - \rho) - \frac{\rho gu}{\gamma KY_e^\gamma \rho_F^{\gamma-1}}, \quad (22)$$

$$\frac{du}{dt} = g\beta \frac{\rho_F - \rho}{k_v \rho_F + \rho} - 3\sigma(\alpha|u| + s) \frac{u k_v \rho_F + \rho_A}{b k_v \rho_F + \rho}. \quad (23)$$

Initial conditions are required for the thermal, specifically, density  $\rho_0$ , radius  $b_0$ , height  $z_0$  and speed  $u_0$ . Equations (19) and (20) can then be integrated numerically (in spatial form) from  $g = 0$  and  $\rho_F = \rho_c = 2.55 \times 10^9 \text{ g cm}^{-3}$  (the density of the star at its center) at  $z = 0$  out to  $z = z_0$ , giving values for  $\rho_F$  and  $g$  at  $t=0$ , completing the set of initial conditions. The system (18)-(23) can then be integrated numerically to obtain the evolution of the thermal.

Again, an equation for the evolution of the Froude number can be derived, here presented in spatial form assuming  $u > 0$ ,

$$\frac{d}{dz} (\text{Fr}^2) = \frac{1}{b} \left[ 2 - \sigma\alpha \text{Fr}^2 \left( 6 + \frac{k_v \rho_F + \rho_A}{k_v \rho_F + \rho} \right) \left( 1 + \frac{s}{\alpha u} \right) \right] - \text{Fr}^2 \left( \frac{4\pi\rho_F G}{g} + \frac{\rho_F g}{3\gamma p_F} - \frac{2}{z} \right).$$

The first term on the right-hand side is similar to equation 9, and indeed reduces to the same with  $s = 0$  and  $\rho = \rho_A$ . The second term accounts for changes in the background stratification, and is a function of  $z$  alone, i.e. it does not depend on the thermal. Assuming  $\text{Fr} \sim 1$ , then the second term varies between approximately  $10^{-9}$  and  $10^{-7}$ . Taking  $1/b$  as an estimate, the first term varies between approximately  $10^{-8}$  and  $10^{-6}$ . This means the ratio of the two terms is about an order-of-magnitude, i.e. the second term is small but cannot be ignored.

### 3.2. Numerical Approach

Full-star simulations of an off-center SNIa ignition were performed in three dimensions by Dong et al. (2011) using the Eulerian, adaptive compressible code, CASTRO, described in Almgren et al. (2010a). The hydrodynamics in CASTRO is based on the unsplit PPM methodology in Miller & Colella (2002). The white dwarf was again modeled using the general equation of state described by Timmes & Swesty (2000), which includes contributions from electrons, ions, and radiation. For these calculations the effects of Coulomb corrections were included from the publicly available version of this EOS (Timmes 2008). Although CASTRO includes a full gravitational potential solver, for the simulations discussed here a simple monopole approximation to gravity was used.

Adaptive mesh refinement in CASTRO follows the same approach as the low Mach number algorithm described in the previous section. The same coarse-grained parallelization strategy is also used, but in conjunction with a fine-grained strategy using OpenMP within the nodes to spawn threads that operate on a portion of the data associated with a patch. Using this strategy, we have been able to demonstrate scalability of CASTRO to more than 200K processors, see (Almgren et al. 2010b).

For the simulations presented here, the star was initialized using a one-dimensional white dwarf model produced with the stellar evolution code Kepler (Weaver et al. 1978). The initial composition was half  $^{12}\text{C}$  and half  $^{16}\text{O}$ . A flame was initialized by creating a bubble of hot ash at a temperature of  $8.5 \times 10^9$  K in pressure equilibrium with the surrounding material, 20 km in diameter located 30 km off the center of the star. The initial sphere was perturbed by a superposition of random spherical harmonics.

The flame was modeled using a thick-flame approximation (see Colin et al. (2000)) with the burning time scale and thermal diffusion adjusted to produce a flame that propagated at  $50 \text{ km s}^{-1}$ . Composition of the ash was determined by a 7 isotope tabular network that enforced nuclear statistical equilibrium for sufficiently high temperatures. The simulation was run with a base mesh of 16 km with 4 levels of refinement by a factor of 2 each. The region around the flame was always forced to be refined to the finest level, so the flame zone had an effective resolution of 1 km. Additional refinement was based on density so that the center of the star was also refined to 1 km resolution with resolution dropping to 4 km at the outer edge of the star.

### 3.3. Results

A series of three-dimensional renderings in figure 6 show the evolution of the thermal in a full star, which follows a similar progression as in the small-scale study. The thermal was initiated with uniform burning over a perturbed sphere, which is very small in comparison with the star. At early times, the thermal burns outwards without rising. Buoyancy accelerates the thermal upwards, which rolls up into a bubble-like structure, which then breaks down due to secondary shear instabilities, with vortical structures distributed across the thermal. The reader is referred to Dong et al. (2011) for more detail. The similarities between figure 6 and figures 1 and 3 suggest that the entrainment-based modeling approach is appropriate for burning thermals in a full star.

We will make two comparisons of the one-dimensional model with the three-dimensional simulation. Firstly, for comparison A, we will set the flame speed  $s$  to zero, consistent with the previous section, and compare different values of the entrainment coefficient  $\alpha$ , and also consider the case where the volumetric expansion term is excluded from the model. In this comparison, the one-dimensional model can only be expected to be applicable once the thermal has become well-developed, which we will take to be  $t \gtrsim 0.1375$  s. Secondly, for comparison B, we will include the flame speed  $s = 50 \text{ km s}^{-1}$  to compare the full one-dimensional model with the three-dimensional simulations, and include the cases with  $s = 0$  and  $\alpha = 0$  for comparison. In this case, it was found that the one-dimensional model was applicable from an earlier time, specifically  $t \gtrsim 0.0413$  s, where it was noted that the vertical speed was zero so the flame burns outwards in a way not described by entrainment alone. All of the one-dimensional cases cannot be expected to be applicable at late times because the expansion of the star is not included in the model, i.e.  $t \gtrsim 0.8175$  s.

To integrate the one-dimensional system of equations, the standard fourth-order Runge-Kutta integrator included with MATLAB was used. Initial conditions for  $t_0$ ,  $z_0$ ,  $u_0$ ,  $b_0$  and  $\rho_0$  were taken from the three-dimensional simulation data, which were evaluated by integrating the data in the same way as the previous section using  $X_C = 0.4$  as the threshold. Time points  $t = 0.1375$  s and  $0.0413$  s were used, respectively for comparisons A and B. Values for  $\rho_F$  and  $g$  at  $z = z_0$  were found by integrating numerically the spatial form of equations (19) and (20) from  $z = 0$ ,  $g = 0$  and  $\rho_F = \rho_c$  to  $z = z_0$ . Equations (18)-(23) were then integrated numerically forward in time until  $z(t) \approx 1500$  km.

The height of the thermal is plotted against radius, time and total mass burned for comparison A in figures 7(a), (b) and (c), respectively. The plus symbols denote the three-dimensional simulation data. The dotted curve denotes the thermal rising without entrainment ( $\alpha = 0$ ), which rises due to buoyancy (faster than in the other cases) and expands due to the change in background stratification only (therefore, much less than in the other

cases). Naturally, the mass burned is constant. The dash-dotted and dashed curves denote  $\alpha = 0.17$  (the value found in the previous section) and 0.3 (for comparison), respectively. The inclusion of entrainment greatly increases the expansion of the thermal (as expected), increasingly so with  $\alpha$ , but even with  $\alpha = 0.3$  the early time evolution does not expand as much with height or burn as much fuel as the three-dimensional data. The later times expand and burn more than the three-dimensional simulation, such that the thermal radius is greater than its height, meaning that it has burned back through the center of the star (see figure 7(a) where the dashed curves are to the right of the solid straight line  $b = z$ ). Both entraining cases match the time-scale more closely, but still appear to rise more quickly than the three-dimensional data. The solid curve denotes  $\alpha = 0.3$  without the volumetric expansion term. In this case, the lack of expansion as the background conditions change means that the buoyancy of the thermal decreases, it becomes neutrally buoyant, and the thermal rise speed drops. The thermal then overshoots the point of neutral buoyancy, it becomes negatively buoyant, and the rise speed becomes negative. The thermal continues to oscillate around a slowly increasing height.

The height of the thermal is again plotted against radius, time and total mass burned for comparison B in figures 7(d), (e) and (f), respectively. Again, the plus symbols denote the three-dimensional data. In this case, the initial condition is taken earlier than comparison A,  $t = 0.0413$  s compared with  $t = 0.1375$  s. The full one-dimensional model, with  $\alpha = 0.17$  and  $s = 50 \text{ km s}^{-1}$ , is shown by the thick solid curve. This is compared with two other cases first with the flame speed turned off  $s = 0$  (dashed curve), and second with entrainment turned off  $\alpha = 0$  (dash-dotted curve). At early times, the thermal is stationary (and therefore not entraining), but burns outwards due to the flame speed  $s$ , so the full model and  $\alpha = 0$  case agree for a short time. As the thermal begins to rise, entrainment becomes more dominant and the  $\alpha = 0$  curve does not expand sufficiently rapidly with height. The flame speed term remains important though, as closer agreement is found here than was found in comparison A with  $\alpha = 0.17$  and  $s = 0$ . The  $s = 0$  case in comparison B does not expand sufficiently quickly at early times, because the thermal is initially stationary, and only begins to entrain as it begins to rise due to buoyancy, which is why comparison A was made with the later initial start time  $t_0 = 0.1375$ . The full one-dimensional model appears to follow the expansion with height of the thermal closely, even as it turns over above  $z \gtrsim 500$  km, but it still over-predicts the spread above  $z \gtrsim 1000$  km, although this is not surprising since the expansion of the star is going to be important by this stage. The full-star model predicts a slightly slower rise speed than in the three-dimensional simulation, but provides the best prediction of the total mass burned. At a height of 1500 km (the extent of the one-dimensional model, beyond which the neglected expansion of the star cannot be ignored), the mass burned in the model is approximately  $0.0840 M_{\odot}$ , which is only about 6% more than at the same height in the

three-dimensional simulation,  $0.0794M_{\odot}$ . We emphasize that this is a semi-analytic result in the sense that the error in the one-dimensional numerical solution is essentially negligible.

### 3.4. Effect of initial conditions

To examine the effect of initial conditions on the evolution of the thermal, a series of calculations were performed using the full one-dimensional model. This emphasizes the benefit of the one-dimensional model, as this study is infeasible in three dimensions. The quantities that were varied were the initial height ( $z_0 = 16, 40, \text{ and } 100 \text{ km}$ ), the initial radius ( $b_0 = 10.2, 25.5, \text{ and } 63.8 \text{ km}$ ), and the turbulent flame speed ( $s = 10 \text{ and } 100 \text{ km s}^{-1}$ ). Note that the cases where  $b_0 > z_0$  were not used. These initial heights and radii are consistent with Zingale et al. (2011), and the turbulent flame speeds are a factor of five slower and two faster than in the previous section, respectively. We note  $100 \text{ km s}^{-1}$  is a little high, but these values are intended to provide lower and upper bounds. The initial rise velocity was taken to be zero, and the initial mass burned taken to be the same value as in the previous section.

The evolution of the thermal height as functions of thermal radius, time, and mass burned are shown in figure 8, where (a)-(c) correspond to  $s = 10 \text{ km s}^{-1}$ , (d)-(f) are for  $s = 100 \text{ km s}^{-1}$ , and the time has been shifted in (b) and (e) so that the data coincide at a height of 800 km. In each case, the thermal initially burns outwards, accelerates upwards, and continues to grow due to burning, entrainment and expansion. The higher flame speed has a pronounced effect at early times as the thermal burns outwards before rising, giving the effect of a larger ignition kernel. For the case where  $z_0 = 16.0, b_0 = 10.2, s = 100$ , the thermal actually burns through the center of the star ( $b > z$ ) and would likely result in a central ignition, which is not recovered by the model as it is assumed to be a point thermal. For large  $z$  the radii of the thermals tend towards similar values, becoming within a factor of about 2 of one another. However, since mass burned depends on radius cubed, this results in values that differ by an order of magnitude (again note that the cases with the largest values of mass burned will have more likely resulted in central ignitions). In general, more mass is burned for larger initial radii, smaller initial heights, and higher flame speed due to the early growth. The thermal height against adjusted time appears to be insensitive to the initial conditions for large  $z$ .

Finally, figure 9 compares the rate of entrainment against the turbulent flame speed for each of the cases. This suggests that once the thermal has become well-developed, i.e. during the buoyant convection stage, the turbulent flame speed plays a diminished role, and the evolution is dominated by the large-scale hydrodynamics responsible for entrainment. We note that the flame speed was included in the model to match the large-scale three-dimensional

simulation which used an assumed turbulent flame speed, so it is possible that the flame speed term is overstated here and it should be even less important during the buoyant convection phase. Furthermore, we emphasize that  $100 \text{ km s}^{-1}$  is somewhat high, and may not be achievable. However, as noted above, the flame speed appears to be important at the early stages of the development, which suggests future studies should focus on the initial transition to turbulence with as detailed a flame model as possible.

#### 4. CONCLUSIONS

The evolution of an off-center ignition in a Type Ia supernova explosion progresses through multiple stages. There is an initial transient as the ignition kernel begins to rise and transitions to turbulent evolution. This is followed by the propagation of the bubble from the center to the periphery of the star by buoyant convection. The final stage results from the interaction of the bubble with the boundary of the star, the outcome of which depends critically on the mass burned by the bubble, which affects the expansion of the star. In this paper we deal with the intermediate stage of turbulent buoyant convection, which we have demonstrated can be well-described by a one-dimensional entrainment model that we have developed. The model is based on the entrainment assumption of Morton et al. (1956) and has been extended to account for both burning and for the change in background stratification of a full star. To account for burning, the Boussinesq approximation was dropped and it was assumed that the entrained fluid was not only mixed, but also burned instantaneously. The density ratio of fuel to ash was then used to account for burning in the volume conservation equation. To account for the background stratification, a polytropic equation of state was used in conjunction with hydrostatic equilibrium, and again the thermal was assumed to equilibrate isentropically and instantaneously to the ambient conditions.

The model was first compared with a high-resolution three-dimensional simulation of a burning thermal in a uniform environment. The burning was observed to occur in pockets distributed evenly across the interior of the thermal, suggesting that the large-scale hydrodynamics, not the local flame speed, controls the rate of mixing and burning. In this simple scenario, the model can be solved analytically to provide power laws for the evolution in the asymptotic self-similar regime. The power laws were in excellent agreement with the three-dimensional data and provided model constants that were carried forward to the full-star model.

The Lane-Emden equation is known not to admit a power-law solution for polytrope order  $n = 3$ , and so the full-star model had to be integrated numerically. The expansion of the rising thermal was captured by assuming that it instantaneously equilibrated to the

ambient pressure, giving rise to another term in the conservation of volume equation. It was found that the inclusion of an extra term in the entrainment was required to account for the large model flame speed in the full-star simulation. However, once all of the components were assembled, the one-dimensional model provided compelling agreement with the three-dimensional simulation. This means that each component of the model (entrainment, expansion, background stratification, and turbulent flame speed) is important for accurately predicting the evolution of the thermal. The success of the entrainment model in predicting the evolution of the burning thermal in a full star again suggests that the dynamics, not the local flame speed, controls the rate of mixing and burning.

There are many aspects that have been neglected, but in particular, the expansion of the star has not been included in the model; hence the model can only be expected to be valid at relatively early times when this expansion is not important. Also, there are other terms in the equation of state that may be important at later times.

The one-dimensional model is computationally inexpensive, especially compared with the three-dimensional simulations, which permitted a study of the effect of initial conditions that would have been infeasible in three dimensions. The data demonstrate that there is some sensitivity to the initial conditions. More mass was burned with a larger initial radius and lower initial height, and a higher flame speed gave the effect of a larger initial kernel resulting in more mass being burned. This means that the very early stages of development are of critical importance in predicting the overall evolution of the thermal. In particular, the initial position and size along with how the early-time flow transitions to turbulence and self-similar evolution will all be extremely important to the total mass burned. Furthermore, the present study does not take into account the background turbulence that results from the large-scale convection present in the star, which may also have significance for the size and position of ignition kernels that can survive.

The authors would like to thank Mike Zingale for his useful discussions. Support for A. J. A. was provided by the Applied Mathematics Program of the Office of Advanced Scientific Computing Research of the U.S. Department of Energy under Contract No. DE-AC02-05CH11231. Support for J. B. B. was provided by the SciDAC Program of the DOE Office of High Energy Physics and the Applied Mathematics Program of the DOE Office of Advanced Scientific Computing Research under Contract No. DE-AC02-05CH11231. At UCSC this research has been supported by the NASA Theory Program NNX09AK36G, the DOE SciDAC Program (DE-FC02-06ER41438), and NSF grant AST 0909129. The computations presented here were performed on the ATLAS Linux Cluster at LLNL as part of a Grand Challenge Project.

## REFERENCES

- Almgren, A. S. et al. 2010a, *Astrophysical Journal*, 715, 1221
- Almgren, A. S. et al. 2010b, in *SciDAC 2010, J. of Physics: Conference Series*
- Aspden, A. J., Nikiforakis, N., Dalziel, S. B., & Bell, J. B. 2008, *Communications in Applied Mathematics and Computational Science*, 3, 101
- Bell, J., Berger, M., Saltzman, J., & Welcome, M. 1994, *SIAM J. Sci. Statist. Comput.*, 15, 127
- Bell, J. B., Day, M. S., Rendleman, C. A., Woosley, S. E., & Zingale, M. A. 2004, *Journal of Computational Physics*, 195, 677
- Berger, M. J., & Colella, P. 1989, *J. Comp. Phys.*, 82, 64
- Colin, O., Ducros, F., Veynante, D., & Poinso, T. 2000, *Phys. of Fluids*, 12, 1843
- Dong, S., Ma, H., Woosley, S. E., Bell, J. B., & Almgren, A. S. 2011, in preparation
- Grinstein, F. F., Margolin, L. G., & Rider, W. J. 2007, *Implicit Large Eddy Simulation* (Cambridge University Press)
- Hillebrandt, W., & Niemeyer, J. C. 2000, *Annu. Rev. Astron. Astrophys.*, 38, 191
- Hoyle, F., & Fowler, W. A. 1960, *ApJ*, 132, 565
- Jordan, G. C., Fisher, R. T., Townsley, D. M., Calder, A. C., Graziani, C., Asida, S., Lamb, D. Q., & Truran, J. W. 2008, *ApJ*, 681, 1448
- Kasen, D., Röpke, F. K., & Woosley, S. E. 2009, *Nature*, 460, 869
- Miller, G. H., & Colella, P. 2002, *Journal of Computational Physics*, 183, 26
- Morton, B. R., Taylor, G., & Turner, J. S. 1956, *Royal Society of London Proceedings Series A*, 234, 1
- Niemeyer, J. C., Hillebrandt, W., & Woosley, S. E. 1996, *ApJ*, 471, 903
- Röpke, F. K., Woosley, S. E., & Hillebrandt, W. 2007, *ApJ*, 660, 1344
- Scorer, R. S. 1957, *Journal of Fluid Mechanics*, 2, 583
- Sim, S. A., Röpke, F. K., Hillebrandt, W., Kromer, M., Pakmor, R., Fink, M., Ruiter, A. J., & Seitenzahl, I. R. 2010, *ApJ*, 714, L52

- Timmes, F. X. 2000, *ApJ*, 528, 913
- Timmes, F. X. 2008, [http://cococubed.asu.edu/code\\_pages/eos.shtml](http://cococubed.asu.edu/code_pages/eos.shtml)
- Timmes, F. X., & Swesty, F. D. 2000, *ApJs*, 126, 501
- Timmes, F. X., & Woosley, S. E. 1992, *ApJ*, 396, 649
- Turner, J. S. 1963, *Quarterly Journal of the Royal Meteorological Society*, 89, 62
- . 1969, *Annual Review of Fluid Mechanics*, 1, 29
- Weaver, T. A., Zimmerman, G. B., & Woosley, S. E. 1978, *ApJ*, 225, 1021
- Woosley, S. E. 2007, *ApJ*, 668, 1109
- Yoon, S.-C., Podsiadlowski, P., & Rosswog, S. 2007, *MNRAS*, 380, 933
- Zingale, M., Almgren, A. S., Bell, J. B., Nonaka, A. J., & Woosley, S. E. 2009, *ApJ*, 704, 196
- Zingale, M., & Dursi, L. J. 2007, *ApJ*, 656, 333
- Zingale, M., Nonaka, A. J., Almgren, A. S., Bell, J. B., Malone, C. M., & Woosley, S. E. 2011, *ApJ*, in preparation

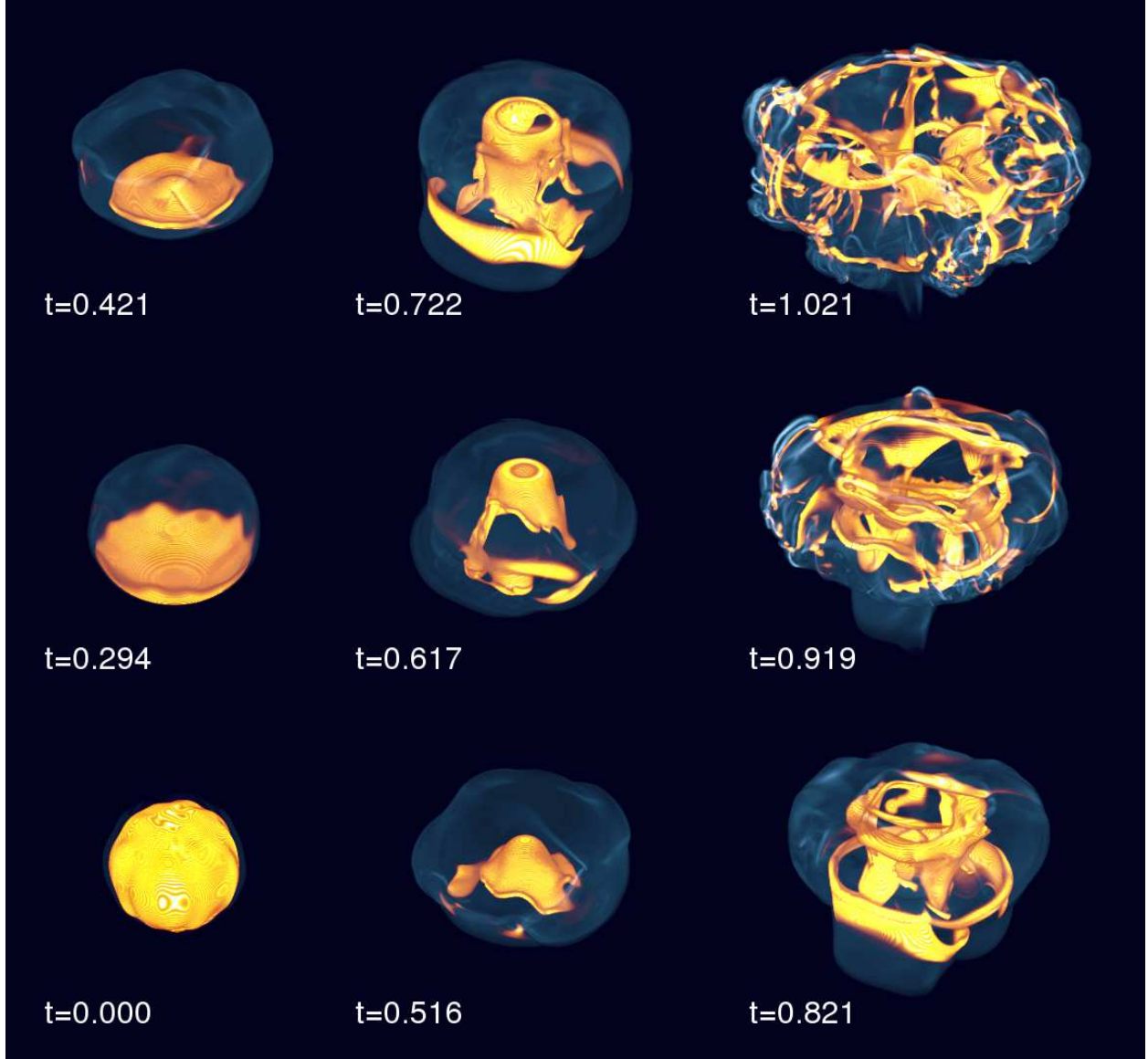


Fig. 1.— Three-dimensional renderings of the early stages of evolution of a burning thermal in a uniform environment. The yellow denotes burning and blue denotes vorticity. All images are at the same scale, where the initial thermal radius was 14 cm. The times corresponding to each image is given in milliseconds (note for context the entire simulated time was 5.6 ms, see figure 3 for evolution after  $t = 1.021$  ms).

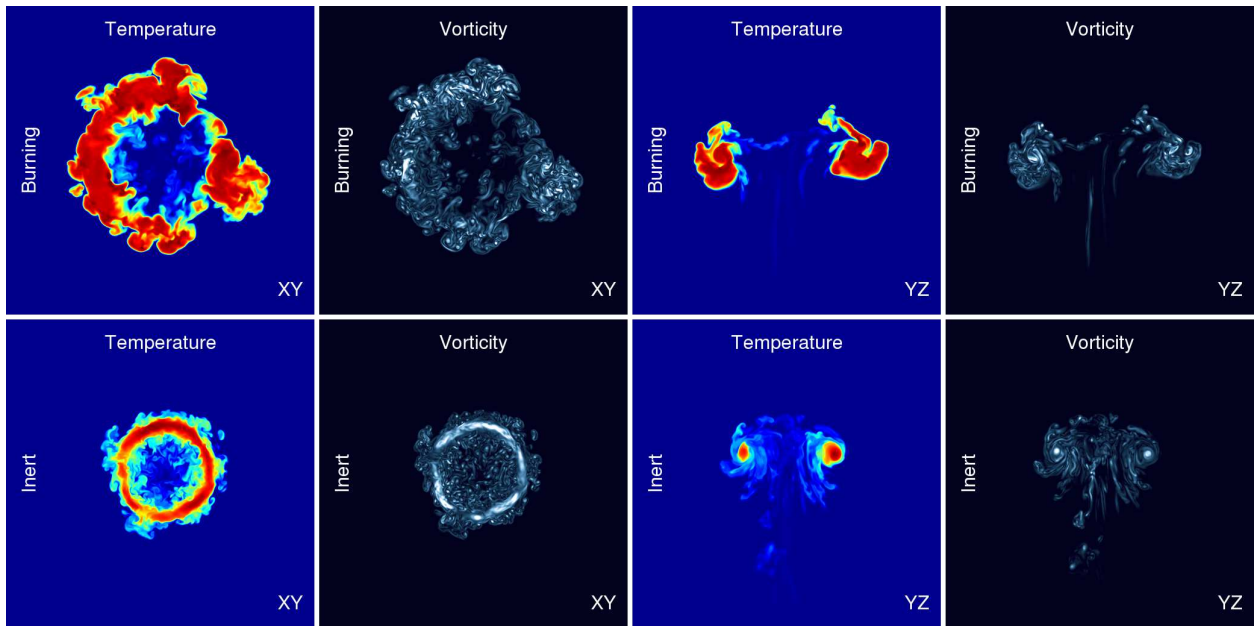


Fig. 2.— Two-dimensional slices from the three-dimensional simulations of a burning thermal (top) and an inert thermal (bottom) in a uniform ambient. For temperature, red is hot, blue is cold. For vorticity, white is high, black is low. The time of the burning thermal is 2.042 ms, and the inert thermal is taken at the same rise height. All images are at the same scale.

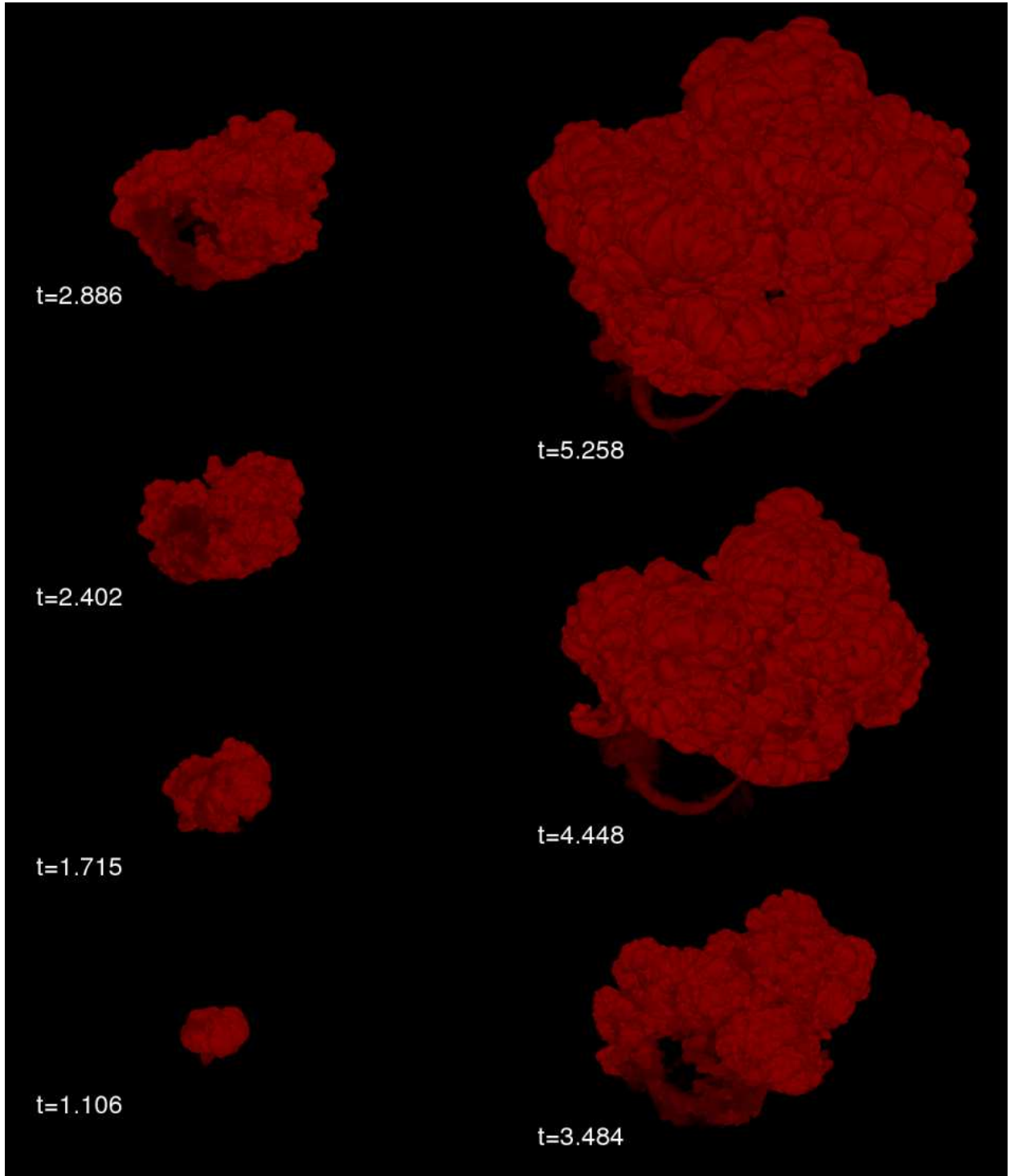


Fig. 3.— Three-dimensional renderings of the later stages of evolution of the temperature of a burning thermal in a uniform environment. All images are at the same scale and times are given in milliseconds. Note the first time corresponds to the latest time shown in figure 1, and highlights the rapid growth of the thermal. At times  $t \lesssim 0.8$  ms, the burning is mainly on the underside of the thermal, but at around  $t \approx 1$  ms, the burning becomes distributed throughout the thermal.

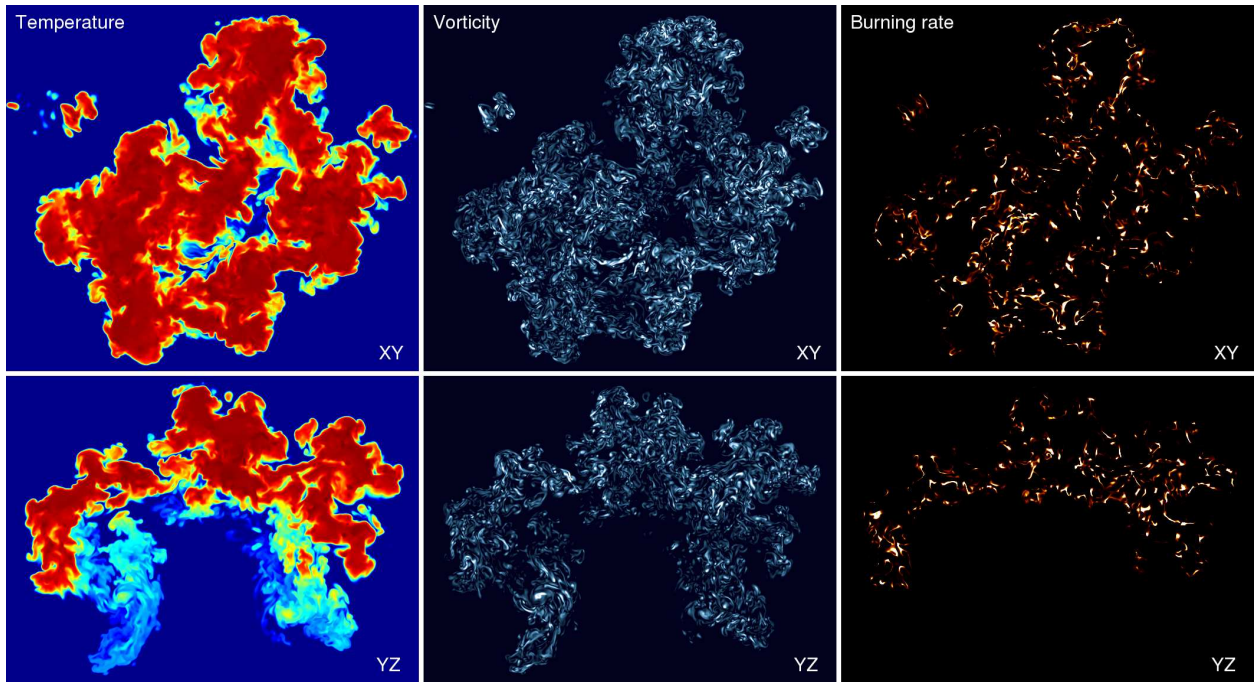


Fig. 4.— Two-dimensional slices from the three-dimensional simulations of a burning thermal in a uniform environment. The top slices are horizontal, and the bottom slices are vertical. The panels left to right are temperature, magnitude of vorticity, and burning rate. All slices are shown at the same scale and time  $t = 3.811$  ms.

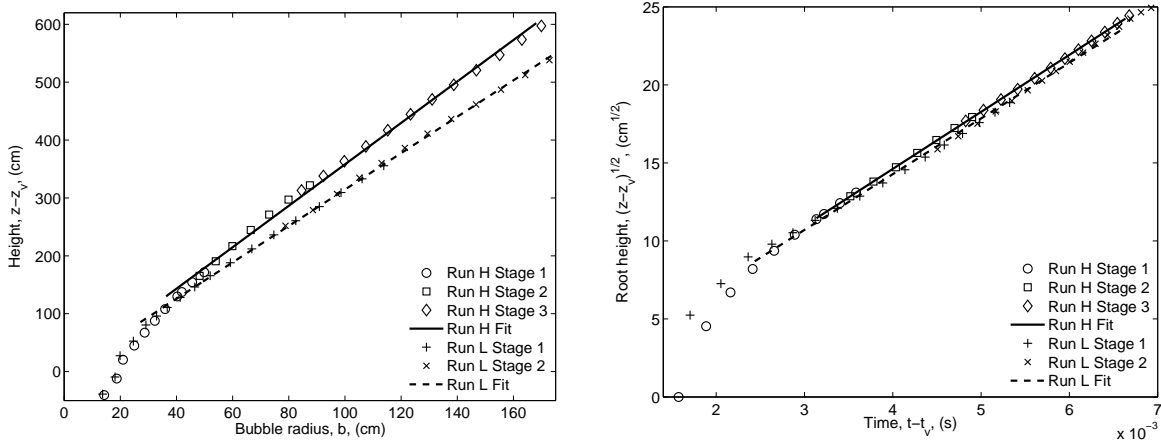


Fig. 5.— (left) Normalized height of the thermal as a function of radius. The thermal is predicted to prescribe a cone, shown by the solid line  $b = \sigma\alpha(z - z_v)$ , where  $\alpha$  was measured through least-squares fitting to be approximately 0.17 for run H and 0.19 for run L. (right) Evolution of the square root of the normalized height of the thermal. After an initial transient, the rise of the thermal appears to rise as predicted; linear growth in  $\sqrt{(z(t) - z_v)} = \sqrt{g'/14}(t - t_v)$  demonstrates the expected quadratic growth. The constant  $\beta$  was determined through least-squares best-fitting to be approximately 0.50.

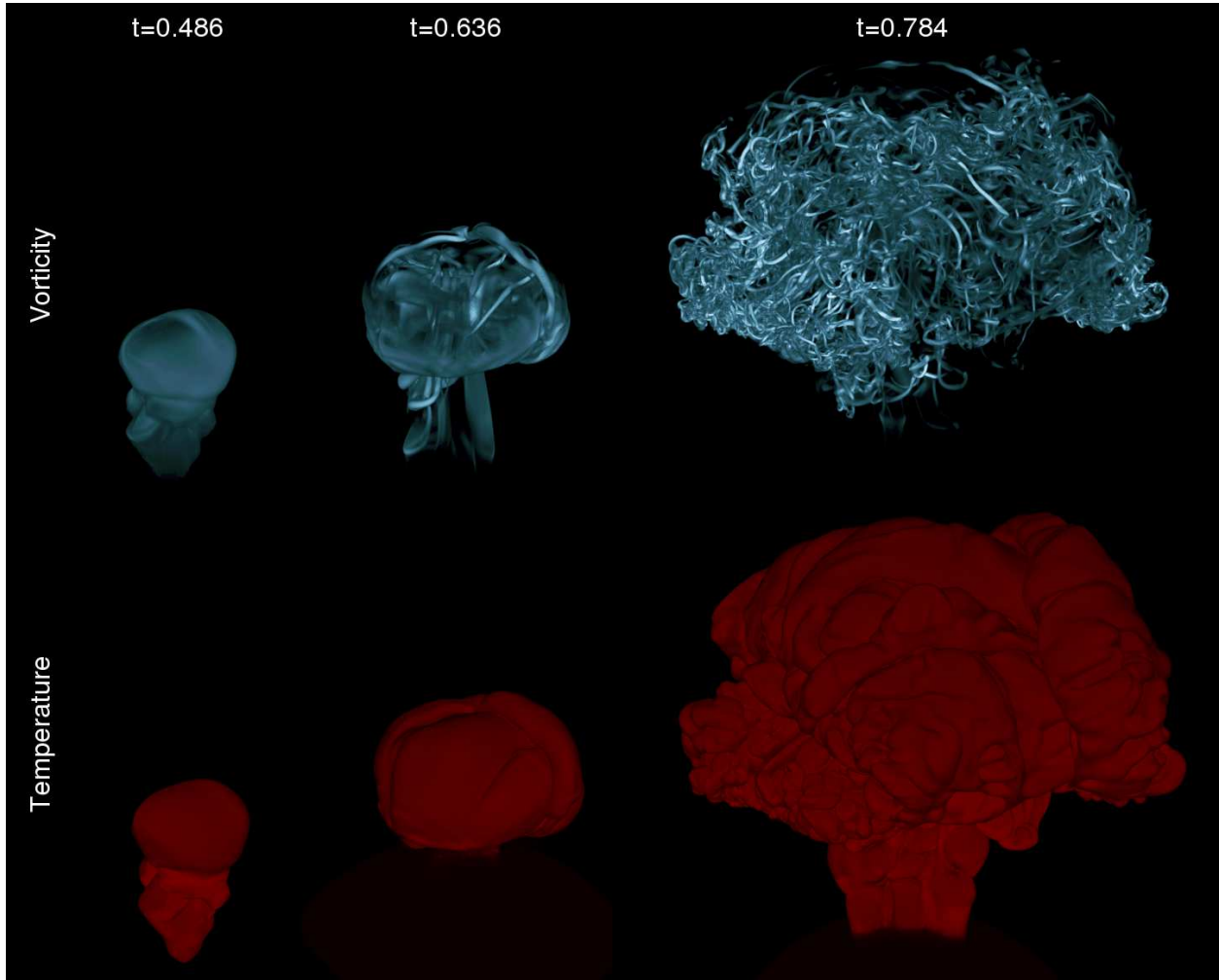


Fig. 6.— Three-dimensional renderings of the evolution of a thermal burning through a full star. Simulation data taken from Dong et al. (2011). Vorticity is shown in blue on the top row, and temperature in red on the bottom row. Times are in seconds. The full-star thermal follows a similar progression to the small-scale study; the thermal rolls up and forms a toroidal structure, which breaks down due to secondary shear instabilities. Further detail can be found in Dong et al. (2011).

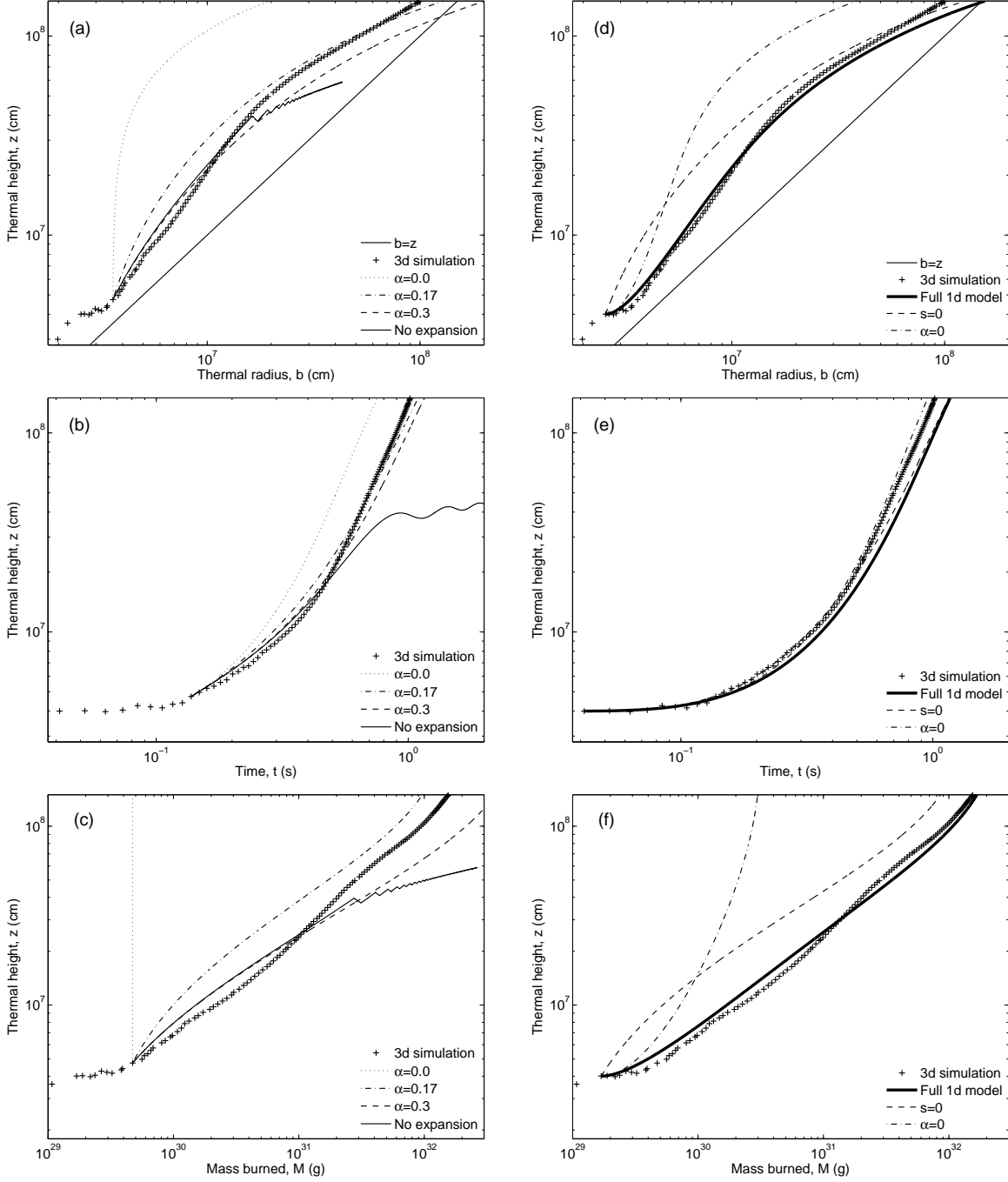


Fig. 7.— Comparisons A (a-c) and B (d-f) of the three-dimensional simulation of a burning thermal in a full star with the one-dimensional model with different combinations of model constants. Comparison A compares the effect of the entrainment coefficient  $\alpha$  and the volumetric expansion term with the flame speed  $s$  set to zero, starting after the thermal has become more well-developed,  $t_0 = 0.1375$  s. Comparison B compares the full one-dimensional model with and without entrainment and the flame speed included, starting from an earlier time  $t = 0.0413$  s.

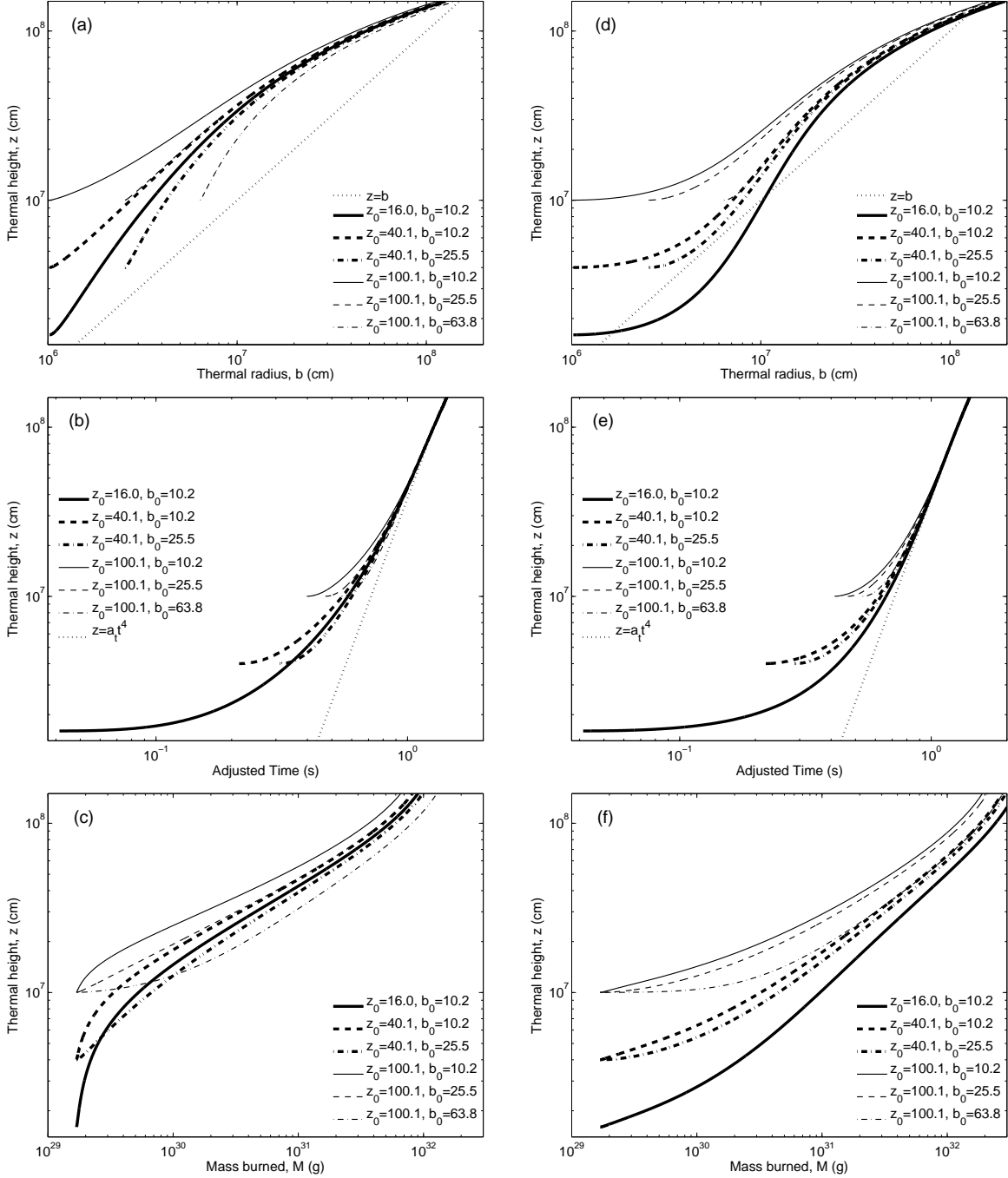


Fig. 8.— Effect of initial conditions on the development of the thermal. (a)-(c) has  $s = 10 \text{ km s}^{-1}$ , and (d)-(f) has  $s = 100 \text{ km s}^{-1}$ . The higher flame speed has a pronounced effect at early times as the thermal burns outwards before rising, giving the effect of a larger ignition kernel. In general, more mass is burned for larger initial radii, smaller initial heights, and higher flame speed due to the early growth.

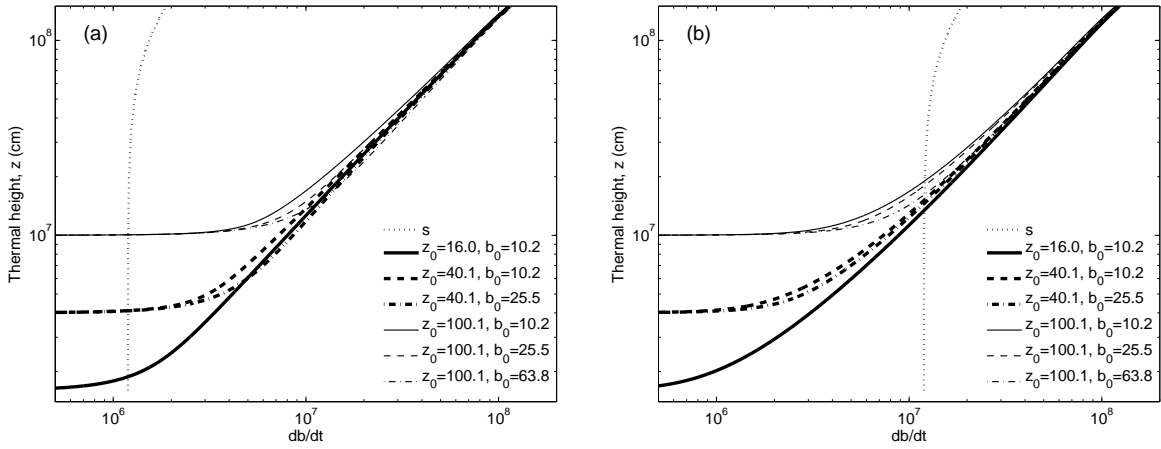


Fig. 9.— Temporal rate of change of thermal radius due to entrainment ( $db/dt = \sigma\alpha|u|$ ) compared against turbulent flame speed ( $db/dt = \sigma s$ ) for (a)  $s = 10 \text{ km s}^{-1}$  and (b)  $s = 100 \text{ km s}^{-1}$ . The effect of flame speed is a function of height alone (through  $\sigma$ ) and is shown by the near vertical dotted line. The other lines correspond to the different initial conditions as in figure 8. Once the thermal has become well-developed, the turbulent flame speed plays a diminished role, and the evolution is dominated by the large-scale hydrodynamics responsible for entrainment. Note that  $100 \text{ km s}^{-1}$  is somewhat high, and may not be achievable, so  $10 \text{ km s}^{-1}$  may be more a relevant comparison.